Generation and Structure–Property Behavior of Novel Liquid Crystalline Foams Produced via a Gas Supersaturation Technique

BRIAN G. RISCH, I-YUAN WAN, JAMES E. McGRATH, and GARTH L. WILKES*

Departments of Chemical Engineering and Chemistry, Polymer Materials and Interfaces Laboratory, Virginia Polytechnic Institute and State University, Blacksburg, Virginia 24061

SYNOPSIS

Linear and star-branched polyoxybenzoate–polyoxyphenoxybenzoate copolymers (POB-*co*-POPB) at a 65/35 molar ratio were synthesized via melt acidolysis using AB-type monomers and branching agents. By controlling the molecular weight and topology of these polymers, both melt processability and solid-state CO_2 gas absorption behavior were enhanced. POB–POPB copolymers with a molar ratio 65/35 showed a glass transition of 143°C and completion of melting at ca. 300°C. POB–POBP copolymers with a systematically increasing branching agent content showed a systematically decreasing peak intensity in wide-angle X-ray diffraction, indicating that increasing branch-point concentration leads to a decrease in liquid-crystal ordering. Star-branched POB–POPB copolymers showed greatly enhanced carbon dioxide gas absorption behavior relative to their linear counterparts. Whereas CO_2 blown foams of linear POB-*co*-POPB produced by the gas supersaturation technique had a relatively high density and showed highly anisotropic bubble growth, well-defined, nearly isotropic foams of star-branched POB-*co*-POPB with a mean cell size from 200 to 400 μ were made using the gas supersaturation technique. Structural features were characterized via scanning electron microscopy, and mechanical properties were determined by indentation testing with a 0.25 in. ball indenter. These LCP foams exhibit relative mechanical properties similar to polystyrene and microcellular polycarbonate foams. A strong inverse relationship was noted between cell size and modulus for liquid crystalline foams with a cell size below 400 μm. © 1994 John Wiley & Sons, Inc.

INTRODUCTION

The motivation to produce polymeric liquid crystalline foams arises from the fact that due to the ease of molecular orientation in these materials under melt flow it is difficult to produce liquid crystalline materials with isotropic or nearly isotropic physical properties. If a polymeric liquid crystalline foam could be produced, the foaming process could produce a more isotropic low-density material, since foaming tends to promote biaxial extension in the cell walls. Furthermore, a liquid crystalline foam could possess the high stiffness characteristic of conventional liquid crystalline polymers on a localized scale combined with more isotropic physical properties on a larger scale. Whereas high molecular orientation is likely to occur in liquid crystalline foams within the cell walls during blowing, if bubbles nucleate and grow isotropically within the material, the resultant structure should possess globally isotropic orientation (Fig. 1). Unlike many conventional foams, these materials might be well suited for high-temperature applications and possibly possess improved barrier properties if the foam is a closed-cell foam. An additional advantage this class of materials offers is that no environmentally hazardous gases are used in the CO_2 supersaturation technique of foam production.

The gas supersaturation process has been recently used to produce microcellular foams of several poly-

* To whom correspondence should be addressed.

Journal of Applied Polymer Science, Vol. 53, 933–951 (1994)
 CCC 0021-8995/94/070933-19

mers including polystyrene and polycarbonate.[1,2] Two variables that are essential in the utilization of the gas supersaturation technique are adequate processability as well as good gas solubility and permeability in the polymer–gas system. In this study, linear and star-branched liquid crystalline polyoxybenzoate–polyoxyphenoxybenzoate copolymers (POB-*co*-POPB) at a 65/35 molar ratio were produced via melt acidolysis using AB-type monomers and tetrafunctional branching agents. By controlling the molecular weight and topology of these polymers, both processability and gas-absorption behavior of these materials were enhanced. The motivation behind using a star-branched topology in this liquid crystalline system was that a star-branched topology might enhance melt processability, and the branch points within the star-branched liquid crystalline polymers (LCPs) might disrupt some of the liquid crystalline order, resulting in improved gas permeability and solubility (Fig. 2). As will be shown, well-defined, liquid crystalline foams of star-branched POB-*co*-POPB with a mean cell size from 140 to 800 μ were produced by the gas supersaturation technique.

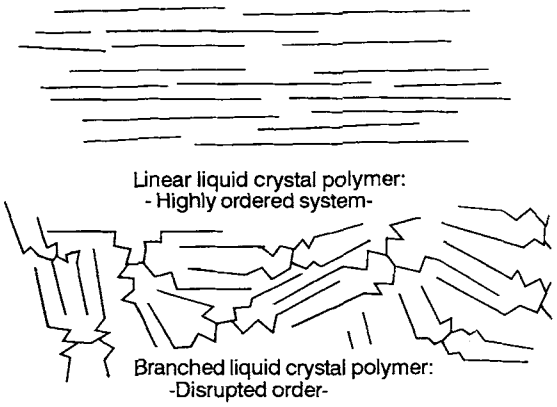

Figure 2 A schematic illustration of liquid crystal disruption of order due to inclusion of branch points.

EXPERIMENTAL

Materials

Although further details of the synthesis of the POB-*co*-POPB polymers utilized will be published later,[3] the synthetic scheme utilized to produce branched POB-*co*-POPB is summarized in Figure 3. To control the branching topology within these polymers, an A–B monomer combined with either A-type endgroups for a linear topology or branch points with A-type functionality for a star-branched topology were used. The molecular weight and topology were controlled by adding the branching or end-capping agents in an appropriate stoichiometric ratio. The predicted molecular weight and topology of the four copolymers used in this study based on stoichiometric ratio are linear (10 K), four-arm (10 K), linear (20 K), and four-arm (20 K) (see Table I). The four-arm (10 K) LCP had a mol fraction of 1.56% branching agent and the four-arm (20 K) LCP had a mol fraction of 0.77% branching agent. Throughout this article, the samples will be referred to according to the topology and molecular weight predicted by stoichiometric offset via the well-known Carothers equation.[4]

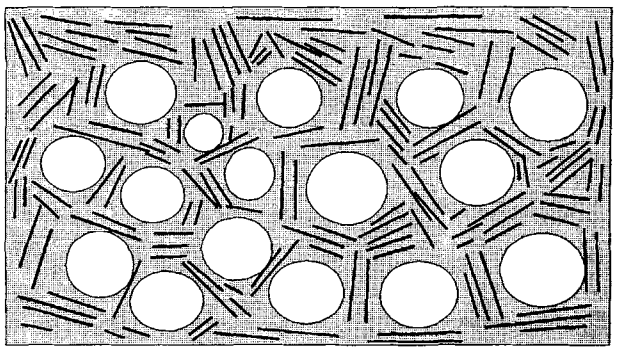

Figure 1 A simplified illustration of globally isotropic orientation in liquid crystalline foams.

Rheological Characterization

These polymers were also characterized according to their melt viscosities. Samples for rheological experiments were compression-molded into 25 × 1 mm discs. All measurements were performed on an RMS 800 shear rheometer. Time sweeps were performed for approximately 5 min at a shear rate of 10 rad/s at 350°C to ensure that the rheological behavior of the materials did not change substantially during the course of the experiments due to chemical reactions (Fig. 4). During this time period, only a slight increase in melt viscosity was noted; however, this change was not significant. Strain sweeps were performed from 0.5% to 5% strain at 350°C, no effect of strain on viscosity on any of the samples was noted. Frequency sweeps were performed from 0.1 to 100 rad/s also at 350°C (Fig. 5). Temperature sweeps were performed from 370 to 300°C at a rate of 3°C/min and at a frequency of 1 rad/s (Fig. 6). Although the data from the temperature sweeps was not in the Newtonian region of the frequency response, data from the temperature sweeps was put

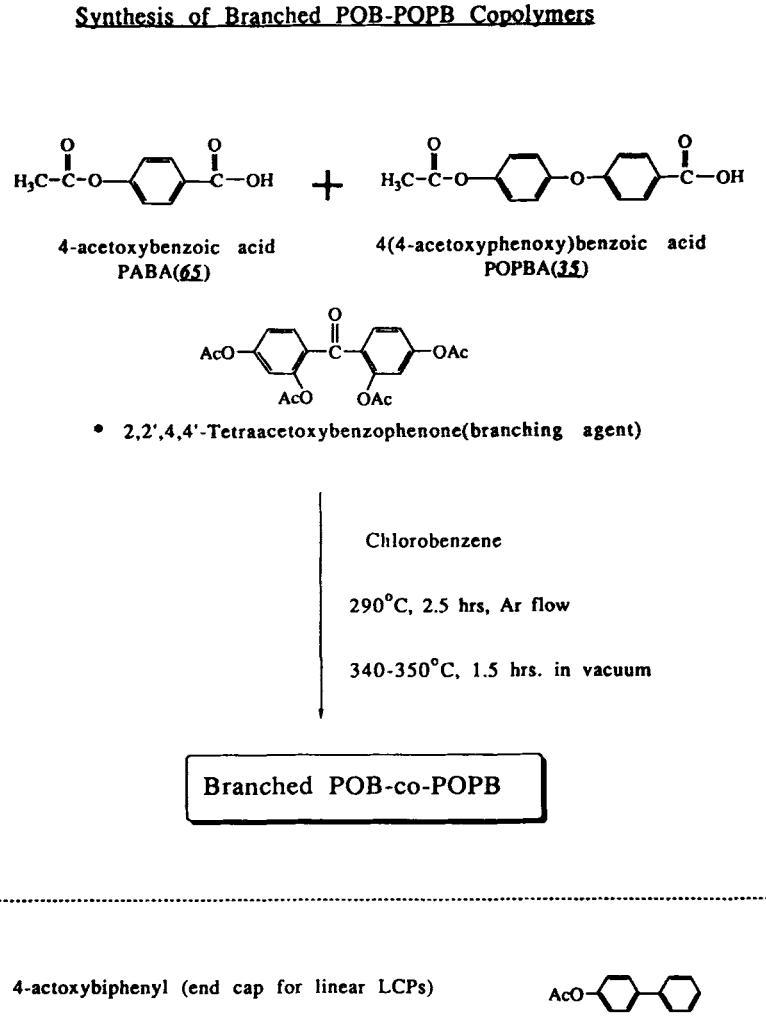

Figure 3 An outline of the synthetic scheme used to produce branched POB-*co*-POPB.

into the form of Arrhenius plots to determine information about the relative molecular weight of the polymers as well as the flow activation energy (Fig. 7).

Foam Generation

As illustrated in Figure 8, the gas supersaturation technique of producing liquid crystalline foams involves three steps: First, compression-molded plaques of POB-*co*-POPB polymers with dimensions of 2 mm thickness and 25 mm diameter were placed in a high-pressure cell filled with Coleman grade 4 CO_2 (99.99% purity) at a pressure of 6500 kPa (950 psi) at 23°C. Samples were periodically removed and weighed on a Mettler balance to monitor mass uptake of CO_2. After 1 week, at which point gas saturation was approached in all samples, these samples

Table I Characteristics of Samples

Sample Designation	Mol % of Branching Agent	Molecular Wt	Topology
Linear (10 K)	0	10,000	Linear
Linear (20 K)	0	20,000	Linear
Four-arm (10 K)	0.77	10,000	Four-arm
Four-arm (20 K)	1.56	20,000	Four-arm

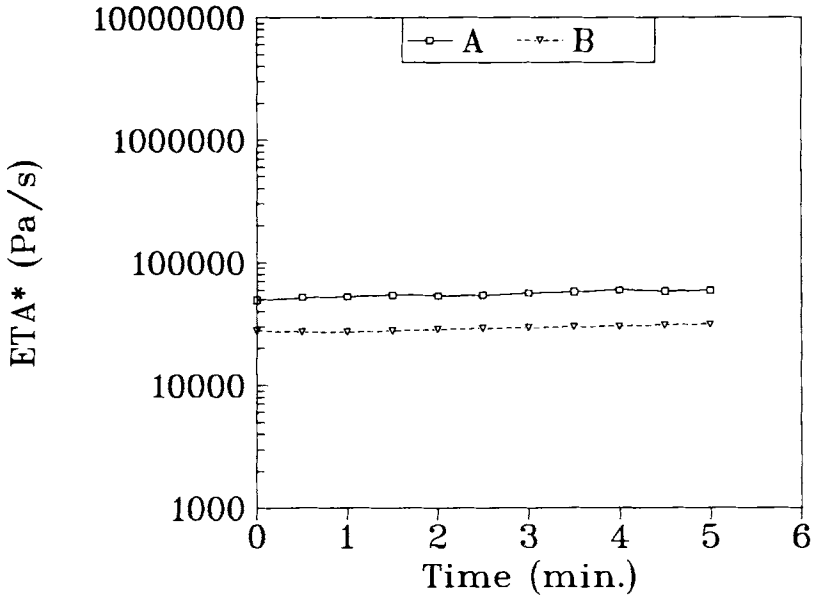

Figure 4 Viscosity–time sweeps at 10 rad/s and 350°C: (A) linear (20K) POB-*co*-POPB; (B) four-arm (10K) POB-*co*-POPB.

were removed from their high-pressure environment and placed in an oven equilibrated at a foaming temperature above the disordering of the LCPs. At this point, bubbles nucleated and grew within the LCP melts. After being held at the foaming temperature for 60 s, the LCPs were removed from the oven and quickly solidified as they cooled to room temperature.

Structural Characterization

All WAXD experiments were performed on a Nicolet diffractometer operating at 40 kV and 30 mA and equipped with a STOE Bragg-Bernatto-type goniometer. CuKα X-rays (1.54 Å) were passed through a graphite monochrometer prior to collimation. Data were collected at 0.05° increments between scatter-

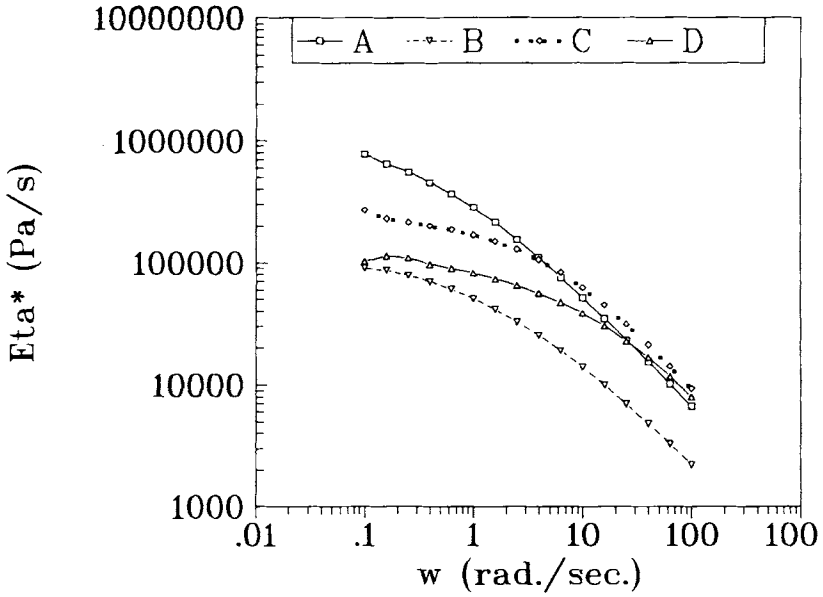

Figure 5 Viscosity–frequency sweeps at 350°C: (A) linear (20K) POB-*co*-POPB; (B) linear (10K) POB-*co*-POPB; (C) four-arm (20K) POB-*co*-POPB; (D) four-arm (10K) POB-*co*-POPB.

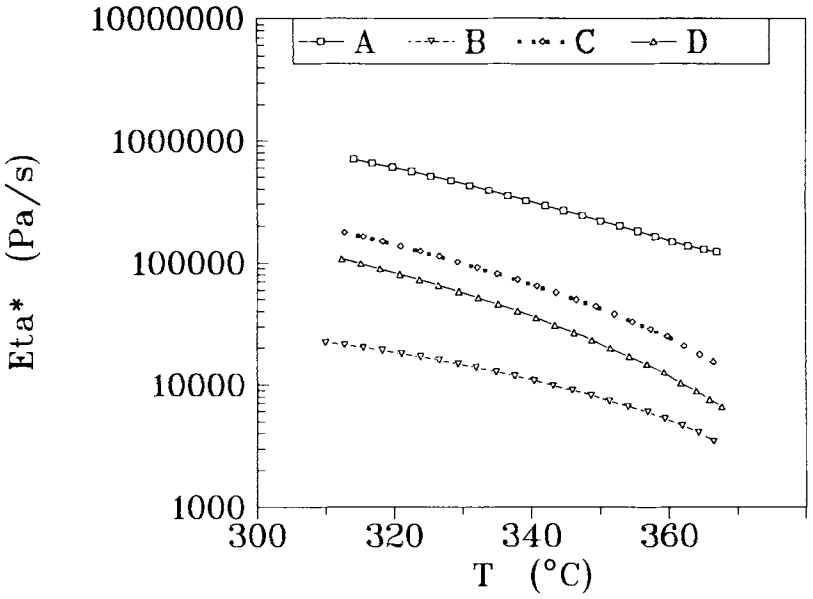

Figure 6 Viscosity–temperature sweeps at 1 rad/s and 3°C/min: (A) linear (20K) POB-*co*-POPB; (B) linear (10K) POB-*co*-POPB; (C) four-arm (20K) POB-*co*-POPB; (D) four-arm (10K) POB-*co*-POPB.

ing angles of 10° and 30°. Data collection and analysis was performed using the Siemens Polycrystalline Software Package.

Samples for polarized optical microscopy (POM) experiments were microtomed from the foams using a razor blade. A Zeiss polarizing optical microscope equipped with a 35 mm camera was used for all POM experiments.

Samples were prepared for SEM by either sectioning with a razor blade (low magnitude) or fracturing them after freezing them in liquid nitrogen for 60 s (high magnitude). Prior to microscopy,

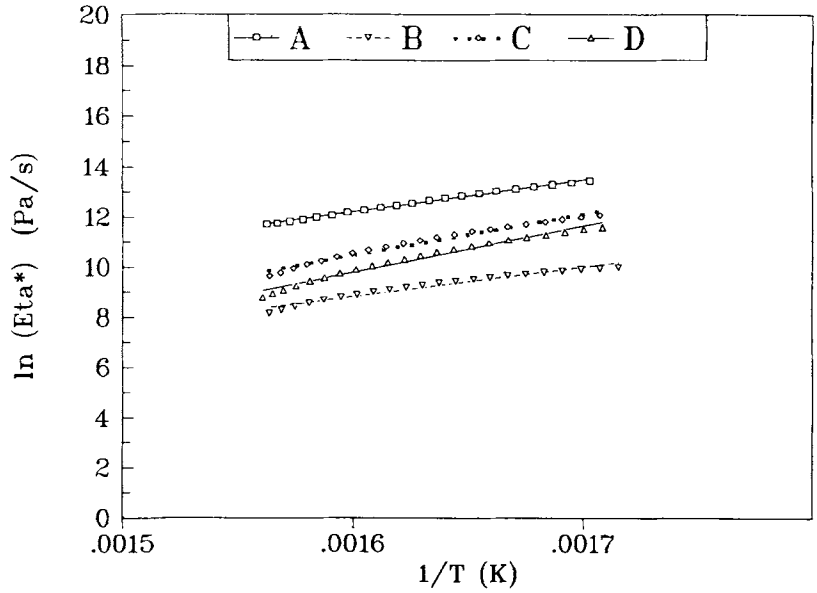

Figure 7 Arrhenius plots obtained from temperature dependence of viscosity: (A) linear (20K) POB-*co*-POPB; (B) linear (10K) POB-*co*-POPB; (C) four-arm (20K) POB-*co*-POPB; (D) four-arm (10K) POB-*co*-POPB.

samples were sputter-coated with gold to a depth of ca. 200 Å in a BioRad E5400 high-resolution SEM sputtercoater. All SEM experiments were performed on a Cambridge Instruments Stereoscan 200 scanning electron microscope set at an operating voltage of 15 kV.

Mechanical Testing

Indentation testing was performed on a Model 4505 Instron mechanical tester interfaced to a Mackintosh computer. The test geometry consisted of a steel plate upon which samples would rest and a 0.25 in. stainless-steel spherical ball indenter that was driven into the samples at a rate of 1 mm/s (Fig. 9). The data collected in this geometry are in the form of load on the indenter head, **P**, vs. displacement of the indenter head, **h**. Sample thickness did not vary greatly from a mean value of approximately 3 mm, so that the strain rate in each case varied little from sample to sample. To ensure homogeneity within each sample and reproducibility of experimental results, each sample was indented in three locations. All tests were performed at 23°C.

DATA ANALYSIS

Rheological Behavior

The behavior of both linear and star-branched polymers has been explained by the entanglement coupling model for polymer melts. At temperatures well above the glass transition temperature, the zero shear viscosity of a polymer may be represented by[5,6]

$$\eta_0 \equiv M^{\alpha}[\zeta(T)] \equiv M^{\alpha}[\zeta_0(T)]^{\{1/[1-n(f)]\}} \quad (1)$$

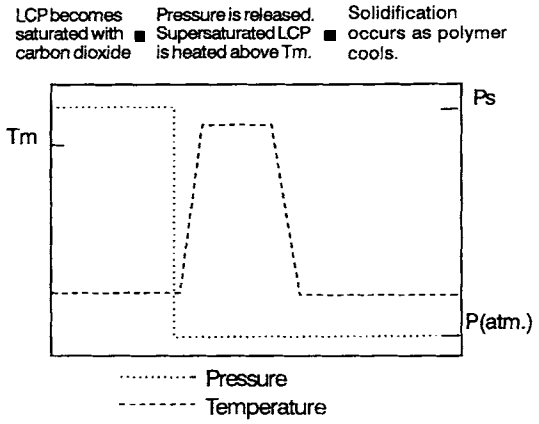

Figure 8 A schematic of the supersaturation process used to produce liquid crystalline foams.

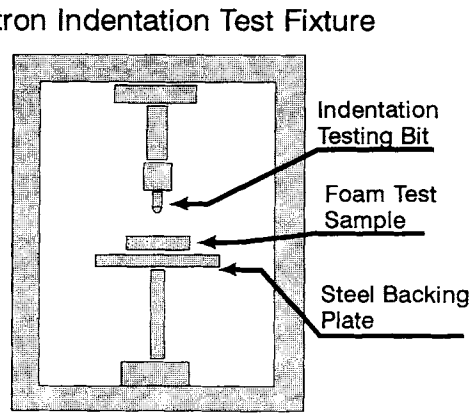

Figure 9 A schematic of the Instron indentation test fixture.

where the monomeric friction factor, $\zeta(T)$, can be expressed in the Arrhenius form as

$$\zeta(T) = Ce^{E_a/\{[1-n(f)]RT\}} \quad (2)$$

where $n(f)$ is the coupling parameter. Ngai and Plazek[5] showed that the primitive flow activation energy, E_a, is more a function of bond rotational energies than of topology. Therefore, the coupling parameter, $n(f)$, of linear or star-branched systems may be determined from the temperature dependence of viscosity. A plot of $\ln(\eta)$ vs. $1/T$ has slope E_a^*/R, $E_a^* = E_a/[1 - n(f)]$. Since E_a is essentially a function of bond rotational energy and independent of topology,[5] $n(f)$, a measure of the effective interaction between polymer chains may be determined.

Mechanical Behavior

Gibson and Ashby identified deformation mechanisms within a variety of foams and applied their knowledge in conjunction with simple models of cell structure to arrive at equations relating mechanical properties to a foam's material composition and structural features.[7] Gibson and Ashby based their model of closed-cell foam behavior on two parameters: the density of the foam, ρ^*, relative to that of the solid polymer, ρ_s, and the proportion of material in the cell edges (struts) Φ[7,8] (Fig. 10). The indentation tests performed in this study give a measure of the initial modulus of a foam and a foam's behavior in compressive collapse.

Foam Modulus

The contributions to foam modulus, E^*, for a closed-cell foam come from bending of cell edges, stretching

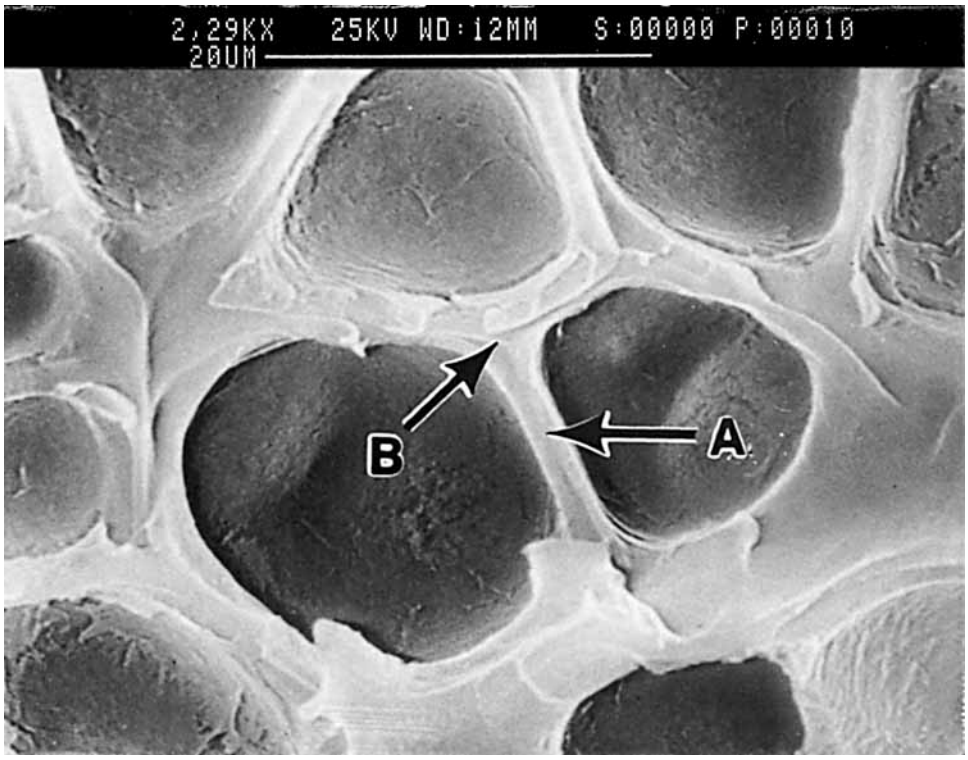

Figure 10 Interpretation of Φ; cell walls vs. cell edges: (A) cell wall; (B) cell edge.

and bending of cell walls, and gas compression. These factors are considered in the following equation:

$$E^* = E_s\{\Phi^2\rho_r^2 + [1 - \Phi)\rho_r] + (P_0/E_s)[(1 - 2\mu^*)/(1 - \rho_r)]\} \quad (3)$$

where $\rho_r = \dfrac{\rho^*}{\rho_s}$; E_s is the modulus of the bulk polymer; P_0, the initial gas pressure in the foam, approximately 1 bar; and μ^*, the Poisson's ratio of the foam, ca. 0.33.[8]

Compressive Collapse

The stress at which elastic collapse takes place, σ_{el}^*, is dictated by the polymer modulus[7]:

$$\sigma_{el}^* = (0.05)E_s(\rho^*/\rho_s)^2 \quad (4)$$

The stress at which plastic collapse occurs, σ_{pl}^*, is governed by the polymer yield stress[7]:

$$\sigma_{el}^* = \sigma_{yield}(0.3)(\rho^*/\rho_s)^{3/2} \quad (5)$$

Equations (4) and (5) define the *onset* of compressive collapse. Elastic collapse occurs when elastic deformation leads to cell wall collapse, whereas plastic collapse occurs when plastic deformation leads to cell wall collapse. Often, cell wall collapse involves both plastic and elastic deformation. Post-collapse behavior is more complicated, but the rise in stress above the collapse value, $\Delta\sigma^*$, may be given as a function of initial gas pressure and strain[7]:

$$\Delta\sigma^* = P_0\epsilon/(1 - \epsilon - \rho^*/\rho_s) \quad (6)$$

Mechanical Testing

A comparison between the raw data obtained from mechanical testing may be obtained by placing data in the form of average applied indenter pressure (stress) vs. a quantity representative of strain. To do this, the contact diameter, $\mathbf{d} = \mathbf{2a}$, is computed from the indenter penetration, $\mathbf{h}$, by

$$\mathbf{d} = \sqrt{(D\mathbf{h} - \mathbf{h}^2)} : \mathbf{h} \leq D/2 \quad (7)$$

$$\mathbf{d} = D : \mathbf{h} \geq D/2 \quad (8)$$

where D is the diameter of the ball indenter. The average stress is calculated from

$$\sigma = \mathbf{P}/A_c = 4\mathbf{P}/\pi\mathbf{d}^2 \quad (9)$$

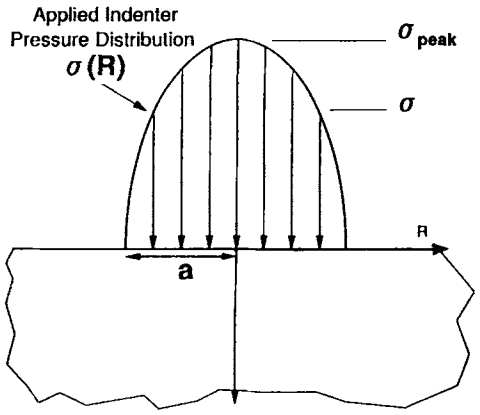

Figure 11 The load distribution produced by a spherical indenter.

indenter (Fig. 11). The load distribution, however, no longer remains parabolic after cell wall collapse. The peak value of stress occurs at the center of the indenter; it has a value $\sigma_{peak} = 1.5\sigma$.[9] The strain, in this case, is represented as the ratio of penetration depth, **h**, to sample thickness, due to the fact that the sample thickness is on the order of the size of the indenter radius. The Young's modulus of the material may be estimated by the following equation that describes the elastic contact behavior developed by Hertz for a spherical indenter[10]:

$$\mathbf{E} = (3\pi/4)\sigma/\epsilon \qquad (10)$$

RESULTS AND DISCUSSION

Rheological testing was performed on these samples to extract information about how adding the branching agent affected the interchain interactions in the polymer melt as well as to extract relative information about the molecular weight of these polymers since GPC experiments could not be performed due to their insolubility—recall Figures 5 and 6. The decreased frequency dependence of star-branched POB-*co*-POPB on viscosity relative to that of linear POB-*co*-POPB is not surprising since recent studies have shown that the relaxation spectra of star-branched polymers are broader than those for linear polymers.[11] The broadened relaxation spectra and exponential dependence of viscosity on arm length for star-branched polymers are attributed to modes of diffusion based primarily on chain retraction.[11-13] The differences in temperature dependence between linear and star-branched polymers is likely due to competition between chain retraction and constraint release. Watanabe et al. showed that in low molecular weight star-branched polymers the characteristic relaxation time associated with constraint release can be comparable to that for the terminal chain retraction mode, i.e., constraint release may have a significant contribution to the viscoelastic response of low molecular weight star-branched polymers.[14] This picture is complicated by the fact that our system may possess liquid crystalline ordering as well. These phenomena may also be responsible for the slightly nonlinear response at high temperatures in the Arrhenius plots. Noting the nonlinear response at higher temperatures, Arrhenius slopes and intercepts were obtained from the data in the 310–350°C range for the linear polymers and from the 310–335°C range for the star-branched polymers—recall Figure 7. Although all the samples did not show zero-shear viscosity behavior at the strain rate used, 1 rad/s, regression analysis combined with equations (1) and (2) can provide at least semiquantitative information about molecular weight and flow activation energy.

Regression analysis in these regions produced R^2 values of at least 0.99, indicating that at least in this region the entanglement coupling model describes the molecular dynamics in this system well. The greater than exponential dependence of viscosity on temperature observed in the star-branched polymers at higher temperatures is likely due to a mechanism of diffusion with a higher activation energy such as constraint release[14] or to the loss of liquid crystalline

Table II Parameters Determined from Arrhenius Plots

Sample Designation	Arrhenius Intercept	E_a^* (kcal/mol)	Relative Molecular Weight
Linear 10 K	−8.7 ± 0.1	17.4 ± 0.8	1
Linear 20 K	−7.93 ± 0.05	20.0 ± 0.3	2.15
Four-arm 10 K	−10.2 ± 0.1	20.1 ± 0.8	0.23
Four-arm 20 K	−8.0 ± 0.1	18.7 ± 0.8	1.95

ordering. A significant increase in the slope of the Arrhenius plot was noted in this region. Since a linear fit to the Arrhenius plots reflects diffusion-based modes of reptation, activation energies and intercepts extracted from the high-temperature region are inaccurate. The data extracted from the Arrhenius plots are summarized in Table II. Relative molecular weights for the polymers were extracted from the Arrhenius intercept. Since there is little difference in the Arrhenius slope as a function of topology and molecular weight, this indicates that the flow activation energies of POB-*co*-POPB vary little as a function of topology in this molecular weight range. In each case, the flow activation energy measured in this manner was much greater than that measured for flexible chain polymer in the same manner. The flow activation energies for the POB-*co*-POPB polymers used in this system (ca. 20 kcal/mol.) were approximately three times that measured for linear polyethylene with $\langle Mw \rangle \approx 10^5$ (6.40 kcal/mol)![5] The increased dependence of the Arrhenius intercept on molecular weight may well be partially due to the exponential dependence of viscosity on the number of entanglements per arm for star-branched polymers.[13,14] Nonetheless, the results of the viscosity measurements suggest that the *relative* molecular weights predicted by the stoichiometric offset are consistent with the rheological data.

The extent to which the liquid crystalline order was disrupted within POB-*co*-POPB is evident through the attenuation of the wide-angle X-ray diffraction (WAXD) peak at ~ 20° (Fig. 12). The intensity of this peak systematically decreases with increasing branch-point concentration, indicating that the branch points cause a disruption of the liquid crystalline order. Although the order is disrupted, however, the WAXD patterns still indicate that liquid crystalline order is present, even in the samples with 1.56% branch-point content. The presence of liquid-crystalline ordering in these systems is further supported by the granular texture observed in the POM experiments [see Fig. 13(A) and (B)]. The granular texture characteristic of LCPs was observed in samples with both 0.77 and 1.56% branching agent content.

Differential scanning calorimetry (DSC) scans performed at 10°C/min indicated a decrease in the magnitude of the disordering transition between 280 and 300°C with increasing branch-point concentration (Fig. 14). The decrease in this melting endotherm also suggests disrupted order within the LCPs containing branch points.

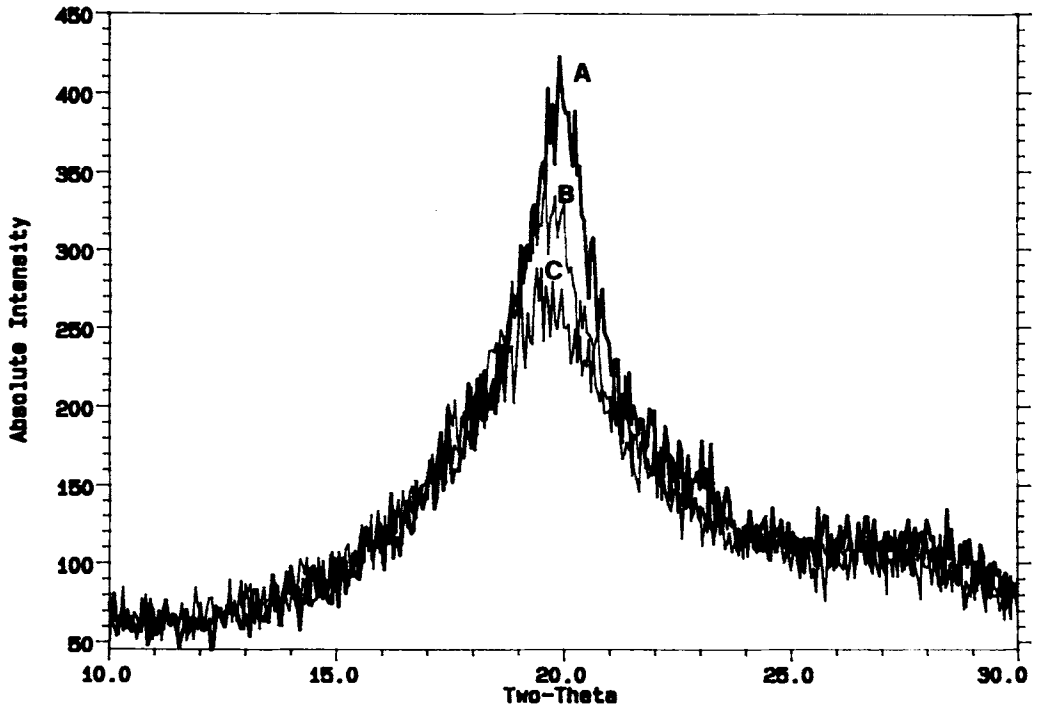

Figure 12 WAXD scans of POB-*co*-POPB; effects of branching: (A) linear (20K) POB-*co*-POPB, 0% branching agent; (B) four-arm (20K) POB-*co*-POPB, 0.77% branching agent; (C) four-arm (20K) POB-*co*-POPB, 1.56% branching agent.

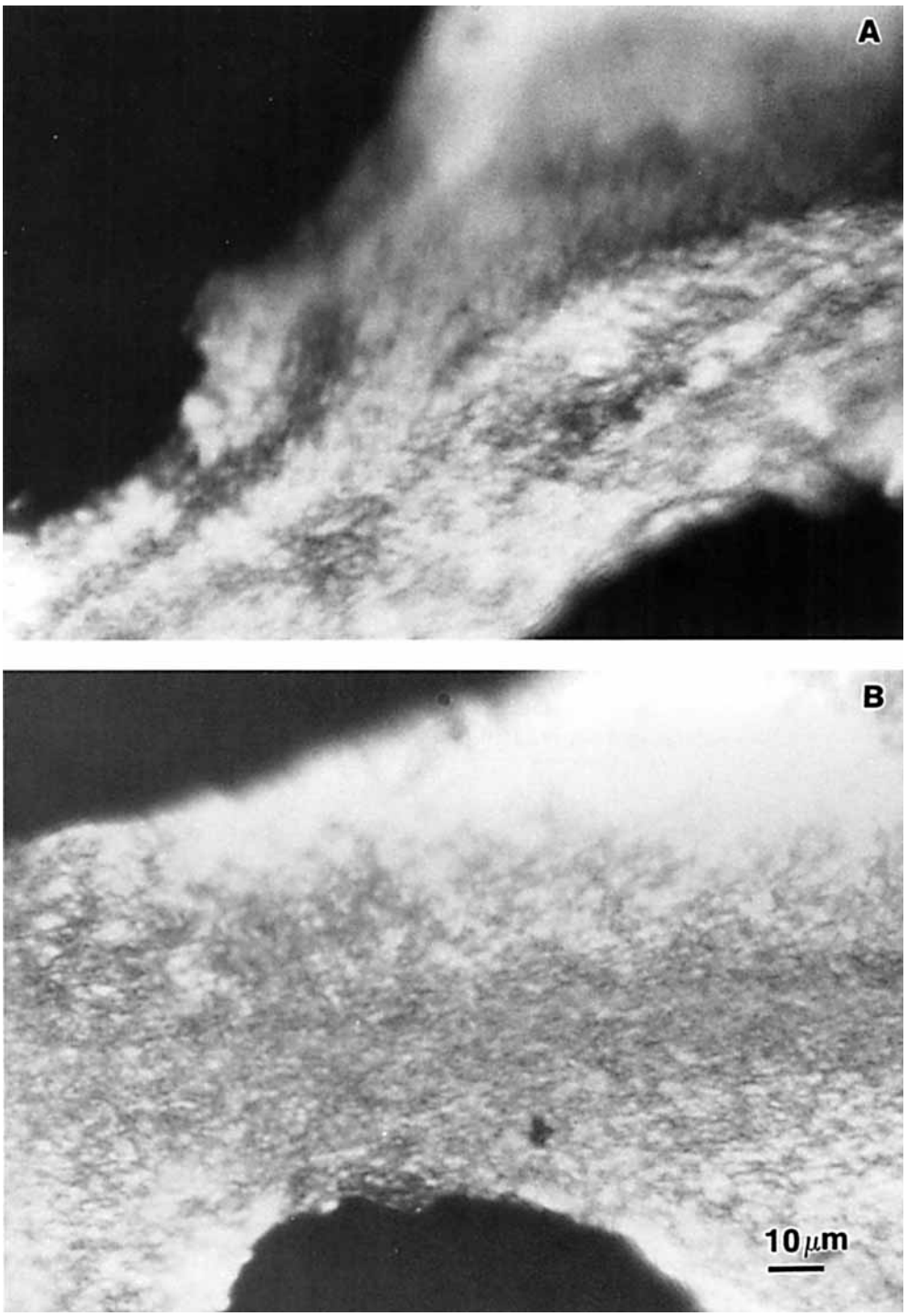

Figure 13 Polarized optical photomicrographs of branched LCPs: (A) four-arm (20K) POB-*co*-POPB; (B) four-arm (10K) POB-*co*-POPB.

The WAXD results suggested that gas permeability and solubility within the branched LCPs might be expected to be enhanced. Figure 15 shows the gas-absorption behavior as a function of molecular weight and topology. The linear LCPs both showed significantly poorer gas-absorption behavior, with the 20 K molecular weight LCP absorbing a mass fraction of only 1.4% CO_2 and the 10 K mo-

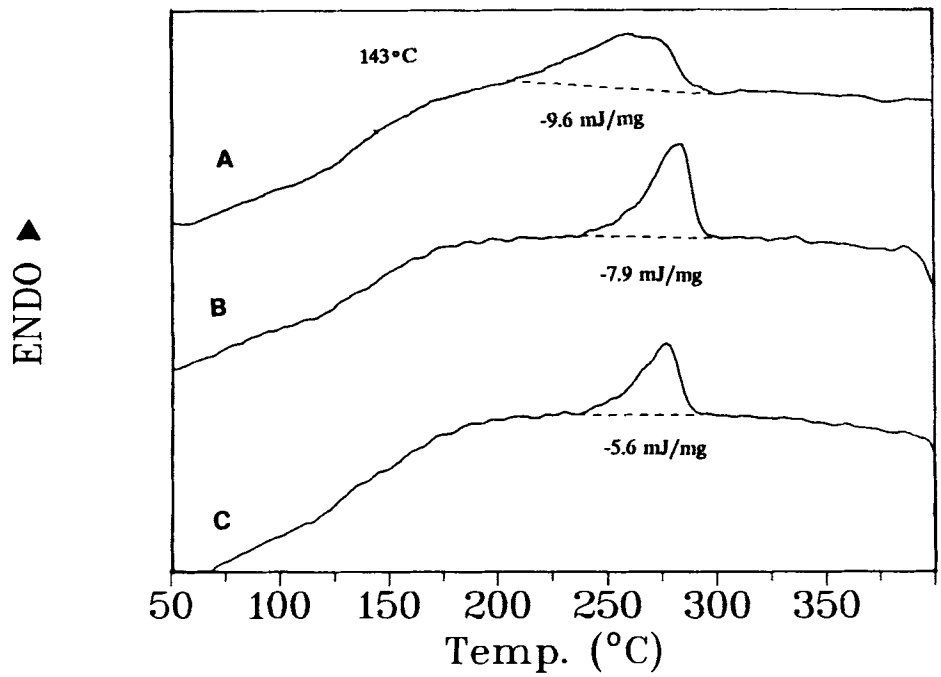

Figure 14 DSC scans of POB-*co*-POPB; effects of branching: (A) linear (20K) POB-*co*-POPB, 0% branching agent; (B) four-arm (20K) POB-*co*-POPB, 0.77% branching agent; (C) four-arm (20K) POB-*co*-POPB, 1.56% branching agent.

lecular weight LCP absorbing a mass fraction of 1.6% CO_2 after 1 week. In the same time period, the 20 K molecular weight LCP with 0.77% branch-point content absorbed a mass fraction of 3.5% CO_2 and the 10 K molecular weight LCP with 1.56% branch-point content absorbed a mass fraction of 7.5% CO_2! Thus, the inclusion of branch points and the resulting disruption of the liquid crystalline order

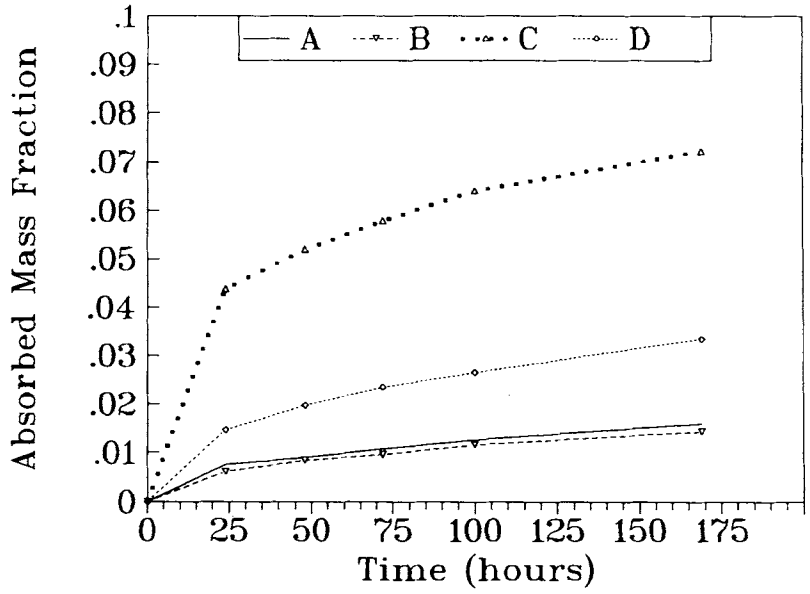

Figure 15 Gas absorption in POB-*co*-POPB; effects of branching: (A) linear (20K) POB-*co*-POPB; (B) linear (10K) POB-*co*-POPB; (C) four-arm (10K) POB-*co*-POPB; (D) four-arm (20K) POB-*co*-POPB.

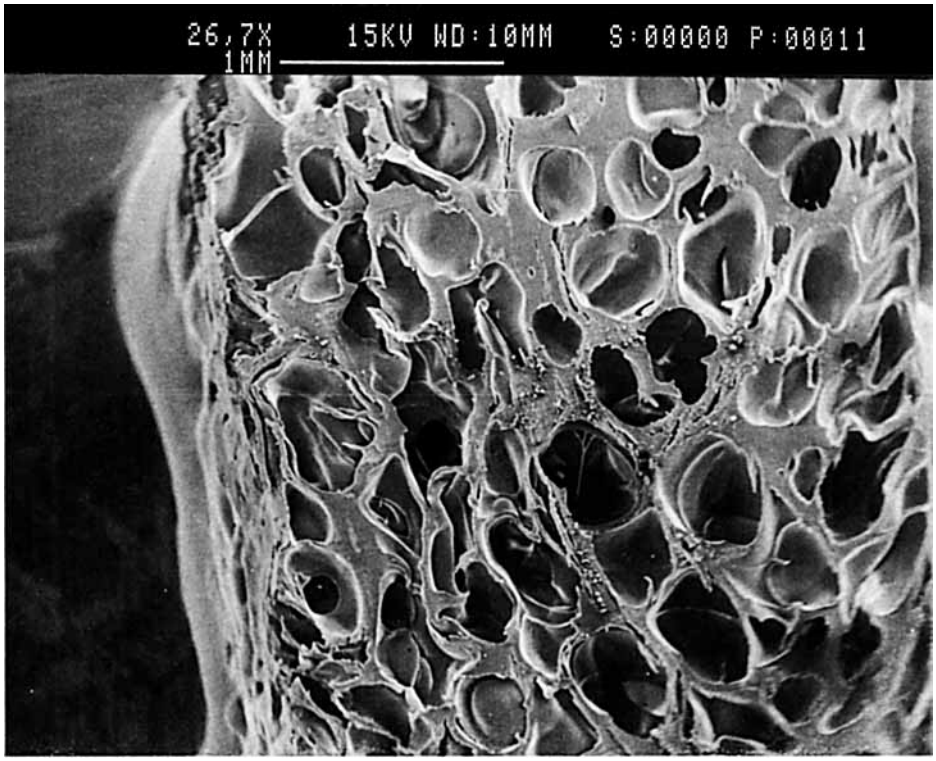

Figure 16 Cross section of a liquid crystalline foam.

dramatically increases the absorption of CO_2 in these POB-*co*-POPB copolymers.

Although the linear POB-*co*-POPB polymers produced foams with relatively high densities and highly anisotropic bubble nucleation and growth, both the 10 K and 20 K molecular weight star-branched POB-*co*-POPB polymers produced well-defined foams with densities from 0.3 to 0.4 g/cc, ca. 30% of the initial density of the compression-molded plaques (1.24 g/cc) (Fig. 16). These foams contained both open and closed cells, although the cells were predominately closed. The nucleation density of bubbles in the four-arm (10 K) foam was greater than that in the four-arm (20 K) foam, and the mean cell size in the four-arm (10 K) foam was less than half that of the four-arm (20 K) foam. The nucleation density also appeared to increase with increasing temperature in both systems (Fig. 17). A highly anisotropic cell shape near the outer skins of these foams suggests that some molecular orientation that occurred during compression molding may have persisted through the subsequent processing of these materials. The characteristic sheet-like structure of LCPs was clearly evident in the cell walls of the liquid crystalline foams, suggesting that the liquid crystalline order and molecular orientation occurred within the cell walls (Fig. 18). Additionally, optical photomicrographs obtained from microtomed sections of the foams revealed the granular texture characteristic of liquid crystalline ordering in the cell walls [see Fig. 13(A) and (B)].

One of the primary goals of this study was to determine the effects that liquid crystalline order within cell walls has on the mechanical behavior of foams. Since the cell sizes produced in POB-*co*-POPB foams via the gas supersaturation technique varied substantially, the effects of cell size on mechanical properties was also studied. Representative data from indentation tests in the form of stress–strain plots are shown in Figure 19. This figure compares the mechanical response of a POB-*co*-POPB foam (mean cell size = 140 μm) with that of microcellular polycarbonate foam produced by the authors (mean cell size = 10 μm) and that of a standard commercial polystyrene foam produced by DOW (mean cell size = 75 μm). The low values of stress achieved for testing in the polystyrene foam are due to its much lower density (ρ^* = 0.05 g/cc) compared to that of the other foams tested (ca. 0.35 g/cc). None of the foams showed a definite yield point, but all three showed a significant decrease in the slope of the stress–strain curve, indicative of cell wall collapse between 5 and 10% strain.

Whereas the polystyrene and polycarbonate

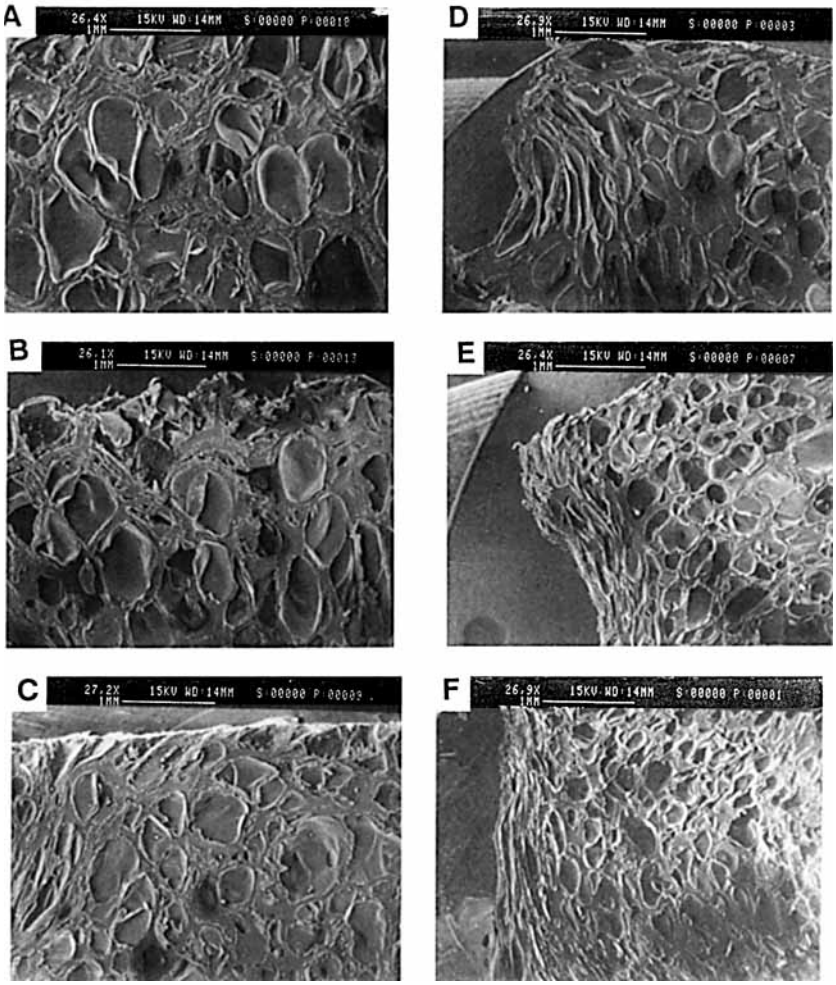

Figure 17 Effects of blowing temperature on nucleation density and cell size: (A) four-arm (20K) POB-*co*-POPB foamed at 310°C; (B) four-arm (20K) POB-*co*-POPB foamed at 325°C; (C) four-arm (20K) POB-*co*-POPB foamed at 350°C; (D) four-arm (10K) POB-*co*-POPB foamed at 310°C; (E) four-arm (10K) POB-*co*-POPB foamed at 325°C; (F) four-arm (10K) POB-*co*-POPB foamed at 350°C.

foams showed the onset of densification at relatively high strains (ca. 70–80%), the POB-*co*-POPB foams appeared to begin densification much earlier in the test. The foams with cell sizes greater than 400 μm appeared to begin densification as early as 40% strain (see Fig. 20). As cell size increased in the POB-*co*-POPB foams, the initial modulus decreased and densification occurred earlier in the test. Both of these trends are attributed to a higher number of irregularities and defects within the foam structure. To compensate for differences in foam densities, the specific moduli (modulus/density) of foams was compared as a function of chemical composition, thermal history, and mean cell size in Table III. The POB-*co*-POPB foams showed specific modulus values between 650 and 1000 MPa $(g/cc)^{-1}$, with a strong dependence on cell size. The effects of foam cell size on the mechanical response of POB-*co*-POPB foams are illustrated in Figure 21. There appears to be a strong inverse dependence between specific modulus and cell size for cells between cells of mean diameter 100–450 μm, but there is little or no noticeable effect of cell size on specific modulus for cells larger than 450 μm. This effect of cell size is not addressed in Gibson and Ashby's approach to describing the mechanical response of foams. An effect of the same magnitude was also noticed by Benning as well as Clutton and Rice in EVA and LDPE foams with densities of 0.045 g/cc, but no explanation was proposed for the observed dependence.[8,15] In our case, it appears that this cell size effect may be due to a combination of factors. Since the POB-

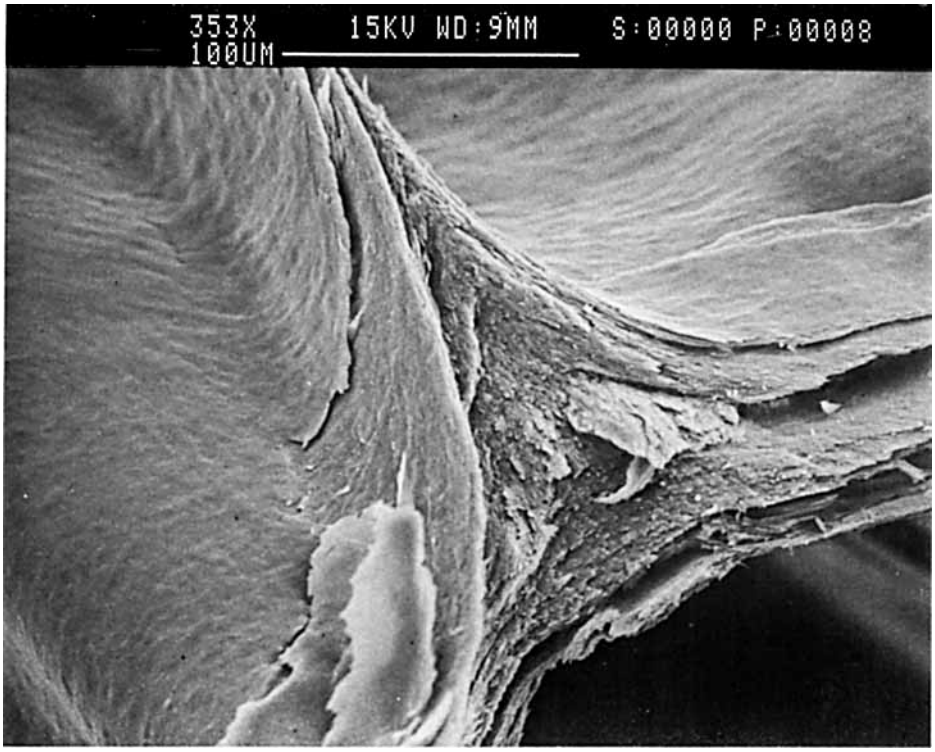

Figure 18 Enlargement of a cell edge showing the sheetlike structure characteristic of LCPs.

co-POPB foams become increasingly irregular in structure with increasing cell size, it is likely that defects and an increasing number of open cells may lead to a decreased initial modulus. Additionally, this effect may be due to a different distribution of material between cell walls and struts as a function of cell size, an effect that *is* accounted for by Gibson and Ashby.

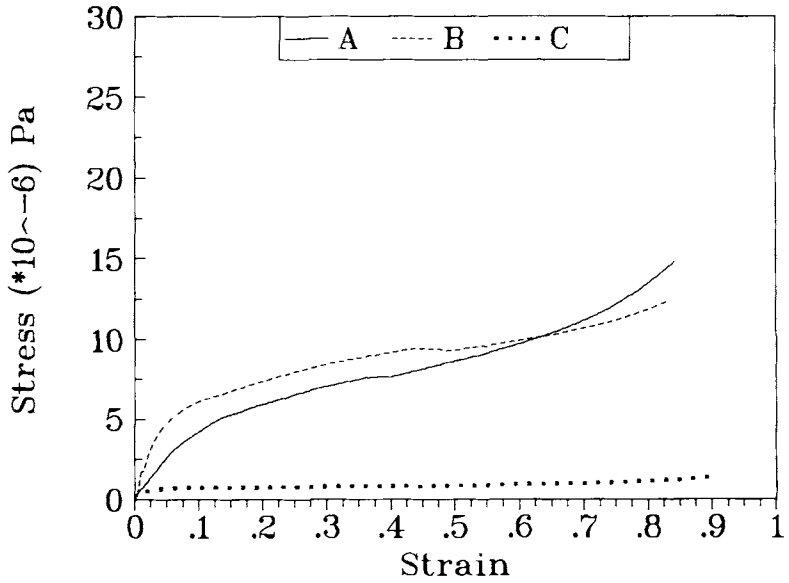

Figure 19 Indentation tests; comparison of different foams: (A) POB-*co*-POPB foam; (B) polycarbonate microcellular foam; (C) polystyrene foam.

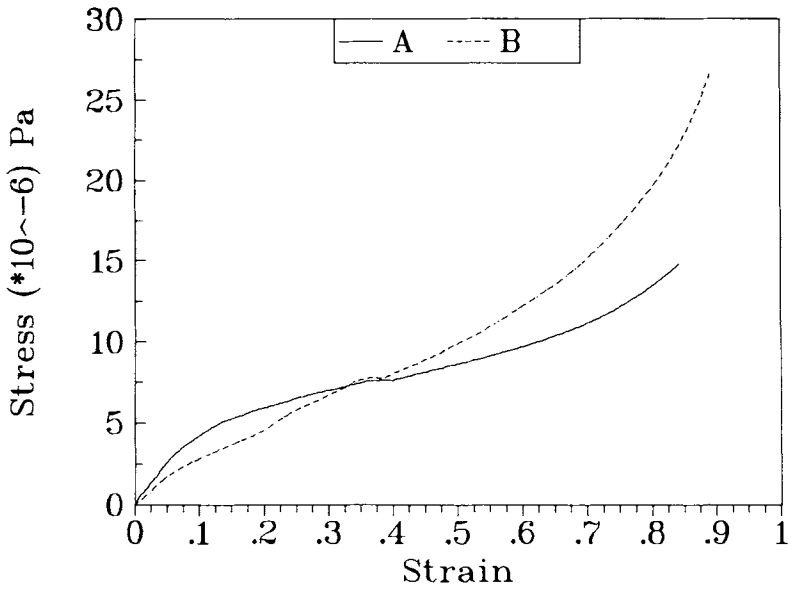

Figure 20 Indentation tests; effects of cell size: (A) four-arm (10K) POB-*co*-POPB foam, mean cell size = 140 μm; (B) four-arm (10K) POB-*co*-POPB foam, mean cell size = 430 μm.

Table IV compares modulus values predicted by eq. (3) with the experimental values. The amount of material in cell edges or struts for a given foam, Φ, is estimated by examination of the respective SEM micrograph, and the modulus of the solid polymers are determined by running indentation tests on standards of solid polymers. Indentation tests were performed on solid polycarbonate, polystyrene, and the POB–POPB copolymers used in this study. From the indentation tests, the initial Young's modulus of the polymers was determined from the initial slope of stress–strain curves. Our results agreed well with modulus values obtained from the literature for polystyrene and polycarbonate.[16] With reasonable estimates of Φ, the predicted values of initial modulus for microcellular polycarbonate and polystyrene foams agree well with the experimental values. The predicted modulus for the foams produced from the four-arm 10 K POB-*co*-POPB also agree well with the experimental values, but the experimental values for the foams produced from the four-arm 20 K POB-*co*-POPB foams fell 40% below the predicted values. The predicted modulus of these foams was greater than that of the foams produced from the four-arm 10 K due to the fact that the experimental values of shear modulus for the higher molecular weight solid polymer obtained by indentation testing was ca. 40% greater.

Table III Specific Modulus and Its Dependence on Foam Composition and Microstructure

Foam	Modulus (MPa)	Density (g/cm^3)	Mean Cell Size (μm)	Specific Modulus (MPa cm^3/g)
Polystyrene	48 ± 1	0.05	75	970 ± 18
Polycarbonate	500 ± 20	0.317	10	1580 ± 60
Four-arm POB-*co*-POPB foams				
(10 K) 350°C	330 ± 10	0.336	140	980 ± 30
(10 K) 325°C	310 ± 15	0.355	240	870 ± 40
(10 K) 310°C	250 ± 30	0.371	430	670 ± 80
(20 K) 350°C	250 ± 30	0.368	430	680 ± 80
(20 K) 325°C	255 ± 50	0.370	650	690 ± 140
(20 K) 310°C	260 ± 50	0.370	800	700 ± 140

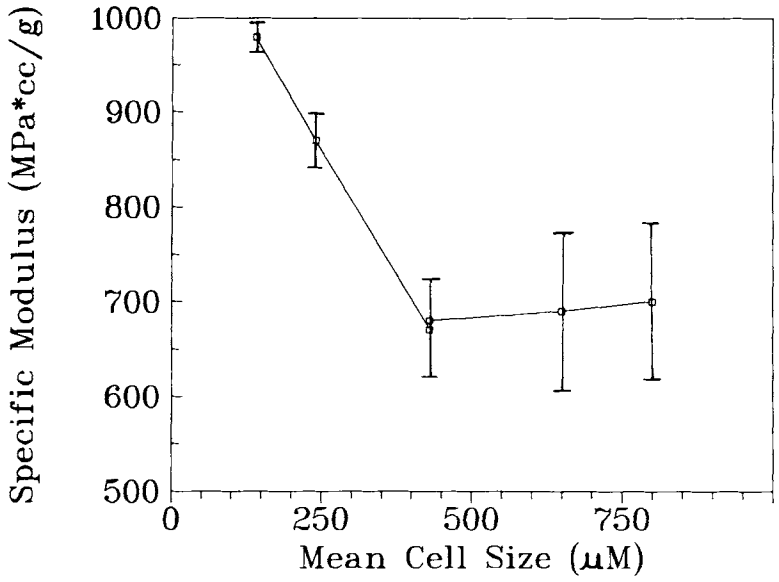

Figure 21 Effect of cell size on specific modulus of POB-*co*-POPB foams.

This may be due to greater ease of molecular relaxation in the lower molecular weight system since molecules in this system are not as likely to be entangled with as many neighbors. Additionally, there may be less molecular orientation in the cell walls of the four-arm 10 K foam. The failure of Gibson and Ashby's model, in these cases, is attributed to the irregularities in structure and high number of structural defects.

The results of indentation testing imply that the effects of cell size on initial modulus may be explained in terms of structural features encompassed by the model of Gibson and Ashby. The POB-*co*-POPB foams generated in this study showed an increase in the amount of material in cell edges with decreasing cell size, leading to an increase in modulus as predicted by eq. (3). Foams with large, irregular cells failed to behave as predicted by eq. (3). Several earlier studies have observed a reduction in the modulus of microcellular foams relative to that predicted by the simple equation[17-20]

$$\mathbf{E}^* = \mathbf{E}_s(\rho^*/\rho_s)^2 \qquad (11)$$

This reduction of modulus was attributed to structural defects within the foams. This simple equation, however, does not account for the structural features of the foam. Figure 22 shows the structure of microcellular polycarbonate and polystyrene foams. Both foams are uniform, apparently defect-free, well

Table IV Comparison Between Observed and Predicted Foam Modulus: Effects of Foam Composition and Structure

Foam	Cell Size (μm)	E^*_{Observed} (MPa)	$E^*_{\text{Predicted}}$ (MPa)	Φ
Polystyrene	75	48 ± 1	48	0
Polycarbonate	10	500 ± 20	507	0.45
Four-arm POB-*co*-POPB foams				
(10 K) 350°C	140	330 ± 10	320	0.5
(10 K) 325°C	240	310 ± 15	302	0.6
(10 K) 310°C	430	250 ± 30	250	0.8
(20 K) 350°C	430	250 ± 30	350	0.9
(20 K) 325°C	650	255 ± 50	350	0.9
(20 K) 310°C	800	260 ± 50	350	0.9

characterized, and consist of essentially all closed cells; however, the cells in the microcellular polycarbonate foam have a significantly greater percentage of material in the cell edges relative to that in the cell walls. If the material in the cell edges is not considered when predicting modulus, eq. (3) overestimates the modulus of microcellular polycarbonate. Conventional foams usually have a very low density with a very small amount of material in the cell edges; thus, eq. (11) does a reasonable job at explaining the behavior. Since the equation developed by Gibson and Ashby considers the effects of structural features as well as foam density, it may applicable for foams regardless of cell size as long as the structural features of the foam are fairly regular.

In explaining the differences in the collapse and densification behavior of the different foams, it is instructive to examine SEMs of the damage left by the indenter (Fig. 23). In both the microcellular polycarbonate and polystyrene foams, foam collapse and densification and collapse occurred through the buckling of cell walls. In the POB-*co*-POPB foams,

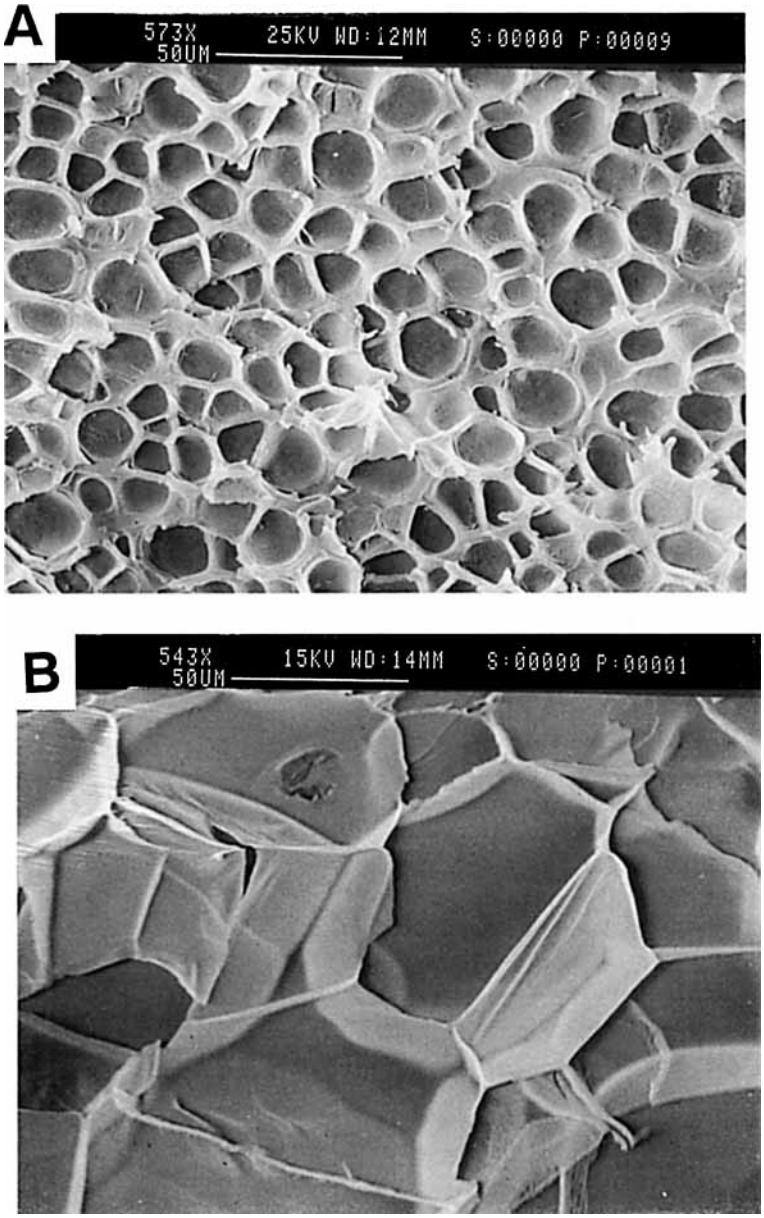

Figure 22 Structural features of microcellular polycarbonate and polystyrene foams: (A) microcellular polycarbonate foam, 573×; (B) polystyrene foam; 543×.

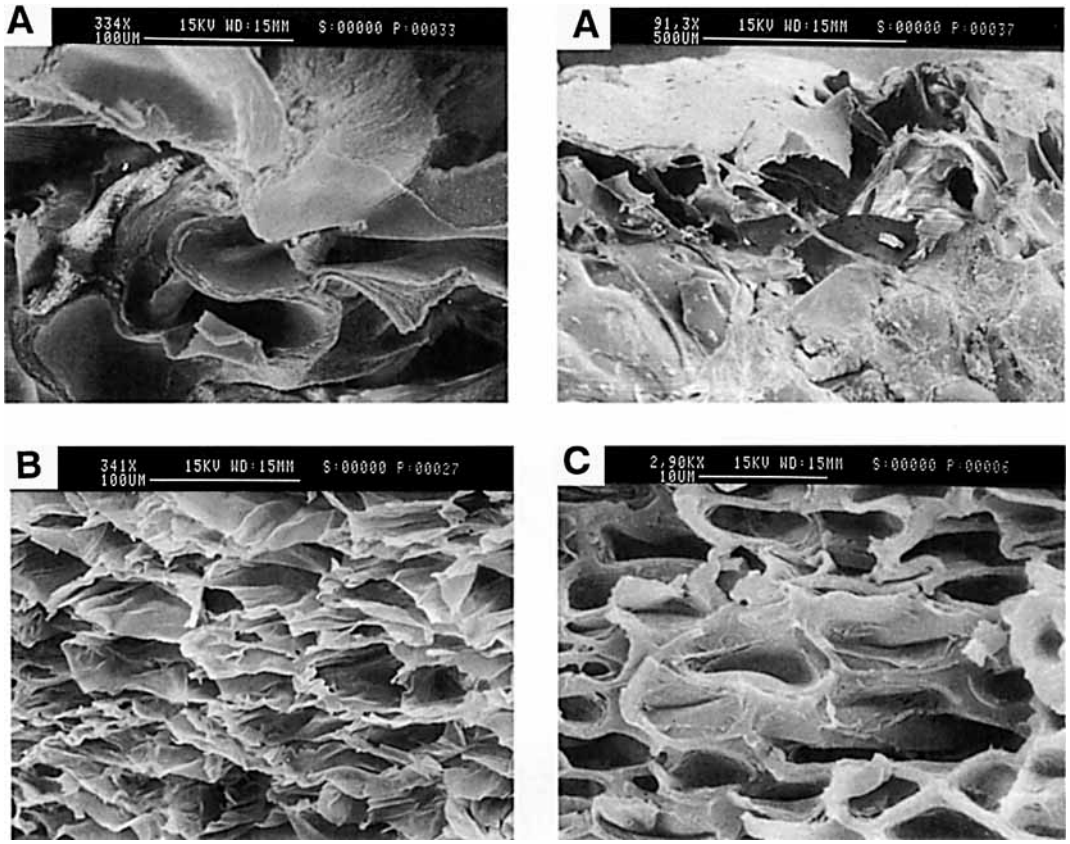

Figure 23 Structural damage produced by indentation testing: (A) POB-*co*-POPB foam; (B) polystyrene foam; (C) microcellular polycarbonate foam.

this buckling of cell walls was also accompanied by cracking in cell walls and at the sample's surface. Crack propagation often leads to failure in conventional liquid crystalline materials; however, in these liquid crystalline foams, cracks are arrested at cell edges, leading to enhanced toughness. This cracking eliminates some of the contribution due to the compression of gas within the cells; however, according to eq. (3), this should only account for about 0.05% of the initial modulus observed for these foams (ca. 47 kPa).

Table V illustrates the plastic and elastic collapse stresses predicted for the foams based on eqs. (4) and (5) compared to the actual collapse stresses observed for the foams studied. Although the *predicted* values of plastic and elastic collapse varied little for the POB-*co*-POPB foams (due to a slight increase in density for the larger cell foams), there was a significant increase in the *observed* value of collapse stress as cell size decreased.

The observed collapse stress of the foams increased from roughly 2 to 3 MPa for the foams with cell size greater than 400 μm to 5 MPa for the foam with a mean cell size of 140 μm. For the POB-*co*-POPB foams with mean cell size over 400 μm, the predicted value for plastic collapse stress were close to the experimentally observed values, although the determination of collapse stress was difficult due to

Table V Comparison Between Observed and Predicted Collapse Stress: Effects of Foam Composition and Structure

Foam	Cell Size (μm)	$\sigma^*_{Observed}$ (MPa)	σ^*_{El} (MPa)	σ^*_{Pl} (MPa)
Polystyrene	75	0.6	3.4	0.06
Polycarbonate	10	6	10.0	2.4
Four-arm POB-*co*-POPB foams				
(10 K) 350°C	140	5.0	10.0	2.5
(10 K) 325°C	240	3.5	11.0	2.8
(10 K) 310°C	430	2–3	12.3	2.8
(20 K) 350°C	430	2–3	13.4	3.0
(20 K) 325°C	650	2–3	13.2	2.9
(20 K) 310°C	800	2–3	13.3	2.9

increased linearity in the stress–strain behavior in these samples. For the polystyrene, microcellular polycarbonate, and POB-*co*-POPB foams with small cells, the observed collapse stress was intermediate between the values predicted for plastic and elastic collapse. It is apparent, since a significant effect of cell size was observed in collapse stress, that eqs. (4) and (5) do not adequately explain the collapse behavior of foams as a function of structure and cell size. The data obtained from indentation tests, however, is unlikely to give a very accurate measure of collapse stress, due to the fact that the load distribution is nonuniform before the onset of collapse and that the load distribution changes as collapse is initiated first in the regions under the greatest stress.

CONCLUSIONS

Closed-cell liquid crystalline foams have been produced by supersaturation with CO_2 gas followed by thermal blowing. To enhance processability and maximize CO_2 absorption, four-arm branching agents were added giving the polymer molecules a star-branched topology. The modification of the topology was found to substantially alter the rheological behavior of these polymers relative to their linear counterparts of comparable molecular weight. A decrease in liquid crystalline ordering due to inclusion of the branch points was observed through both WAXD and DSC experiments. Star-branched POB-*co*-POPB was found to absorb up to 8.5% CO_2 by mass. By varying thermal blowing temperature and molecular weight, foam cell size was varied from 100 to 800 μm. The LCP foams produced by the supersaturation process exhibited mechanical behavior comparable to polystyrene and microcellular polycarbonate foams. The mechanical behavior of the foams was found to agree quite well with the general model proposed by Gibson and Ashby for initial foam modulus of a closed-cell foam if the foams had a fairly regular and defect-free structure. A strong inverse relationship between modulus and cell size was attributed to differences in the amounts of materials in cell edges vs. cell walls and structural irregularities. The collapse stress observed for the foams fell between the values predicted by Gibson and Ashby for elastic and plastic collapse. The results of this study imply that if structural features such as cell size and the fraction of material in cell edges can be controlled, foam properties may be controlled as a function of structure as well as density. This study also illustrates that irregularities and inhomogeneities within a foam's structure lead to decreased initial modulus and yield stress.

The authors appreciate the support of this research by the National Science Foundation Science and Technology Center for High Performance Polymeric Adhesives and Composites at Virginia Polytechnic under Contract Number DMR8809714 as well as the Phillips Petroleum Co. We would also like to thank Will Hartt and Professor Donald G. Baird for assistance in the rheological characterization as well as Jack Lesco and Professor Dave Dillard for assistance in the mechanical testing.

REFERENCES

1. J. E. Martini, F. A. Waldman, and N. P. Suh, *SPE Techn. Pap.*, **28,** 674–676 (1982).
2. V. Kumar, J. E. Weller, and H. Y. Hoffer, in *Symposium on Processing of Polymers and Polymeric Composites,* ASME Winter Annual Meeting, 1990, MD-19, pp. 197–212.
3. I.-Y. Wan, B. G. Risch, G. L. Wilkes, and J. E. McGrath, to appear.
4. W. H. Carothers, *Trans. Faraday Soc.*, **32,** 39 (1936).
5. K. L. Ngai and D. J. Plazek, *J. Polym. Sci. Polym. Phys.*, **23,** 2159 (1985).
6. B. G. Risch, G. L. Wilkes, and J. M. Warakomski, *Polymer,* **34,** 2330 (1993).
7. L. J. Gibson and M. F. Ashby, *Cellular Solids: Structure and Properties,* Pergamon, Oxford, 1988.
8. E. Q. Clutton and G. N. Rice, *Cell. Polym.,* **11,** 429 (1992).
9. J. J. Lesko, G. P. Carman, D. A. Dillard, and K. L. Reifsnider, in *Proceedings of the ASTM Symposium on Composite Materials: Fatigue and Fracture,* 1993, pp. 401–418.
10. H. Hertz, *J. Math. (Crelle's J.),* **92** (1881).
11. L. V. Fetters, A. D. Kiss, D. S. Pearson, G. F. Qnact, and F. J. Vitas, *Macromolecules,* **26,** 647 (1993).
12. P. G. de Gennes, *J. Phys. (Paris),* **36,** 1199 (1975).
13. G. Kraus and J. T. Gruver, *J. Polym. Sci.,* **A3,** 105 (1965).
14. H. Watanabe, H. Yoshida, and T. Kotaka, *Macromolecules,* **25,** 2442 (1992).
15. C. J. Benning, *Plast. Foams,* **1,** 324 (1969).
16. M. J. Howard, Ed., *Plastics: A Desk Top Data Bank,* The International Plastics Selector, San Diego, 1980.
17. J. M. Williams, *J. Mater. Sci.,* **23,** 900 (1988).
18. C. L. Jackson, M. T. Shaw, and J. H. Aubert, *Polymer,* **32,** 221 (1991).
19. J. D. LeMay, R. W. Hopper, L. W. Hrubesh, and R. W. Pekala, *MRS Bull.,* **15**(12), 19 (1990).
20. M. H. Ozkul, J. E. Mark, and J. H. Aubert, *J. Appl. Polym. Sci.,* **48,** 767 (1993).

Received January 29, 1994
Accepted March 2, 1994